Oceanic internal solitary waves in three-layer fluids of great depth

Zi'an Wang[1,2], Zhan Wang[1,2,3*], and Chunxin Yuan[4]

[1]*Institute of Mechanics, Chinese Academy of Sciences, Beijing 100190, China;*
[2]*School of Engineering Science, University of Chinese Academy of Sciences, Beijing 100049, China;*
[3]*School of Future Technology, University of Chinese Academy of Sciences, Beijing 100049, China;*
[4]*School of Mathematical Sciences, Ocean University of China, Qingdao 266100, China*

This paper is mainly concerned with modeling nonlinear internal waves in the ocean of great depth. The ocean is assumed to be composed of three homogeneous fluid layers of different densities in a stable stratified configuration. Based on the Ablowitz-Fokas-Musslimani formulation for irrotational flows, strongly nonlinear and weakly nonlinear models are developed for the "shallow-shallow-deep" and "deep-shallow-deep" scenarios. Internal solitary waves are computed using numerical iteration schemes, and their global bifurcation diagrams are obtained by a numerical continuation method and compared for different models. For the "shallow-shallow-deep" case, both mode-1 and mode-2 internal solitary waves can be found, and a pulse broadening phenomenon resulting in conjugate flows is observed in the mode-2 branch. While in the "deep-shallow-deep" situation, only mode-2 solitary waves can be obtained. The existence and stability of mode-2 internal solitary waves are confirmed by solving the primitive equations based on the MITgcm model.

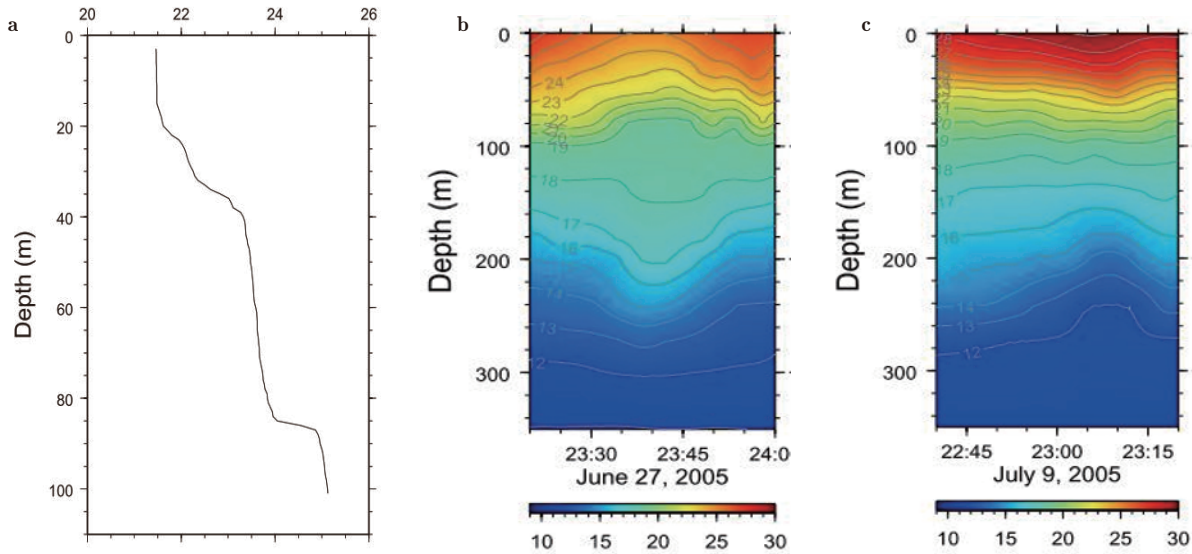Internal wave, Interfacial wave, Solitary wave

1. Introduction

Due to temperature and salinity variations in the vertical direction, the ocean features density inhomogeneity resulting in the pycnocline, a diffusive boundary between the upper lighter fluid and lower heavier fluid. When the pycnocline fluctuates, internal waves, one of the most important phenomena of stratified fluids, appear. Internal gravity waves are ubiquitous in the ocean and are usually induced by tidal or other currents in the condition of significant bottom topography. Early famous field observations were carried out by Perry and Schimke [1], who found groups of internal waves up to 80 m high and 2000 m long on the main thermocline near Sumatra and followed by Osborne and Burch [2], who found internal solitary waves generated by tidal currents on the chain of the Andaman and Nicobar Islands. Compared with surface gravity waves, internal waves have a longer time scale and larger amplitude due to the much smaller density difference across the pycnocline than the air-water interface. Hence, they significantly impact people's daily production and life, ocean engineering, marine military, underwater communication, etc. For example, the current induced by internal waves can affect the mass and energy transport of the oceanic ecosystem and have a considerable impact on offshore platforms and underwater production facilities.

Many studies of internal waves use a simple mathematical idealization, which considers the pycnocline as a sharp interface between two immiscible and homogeneous fluids of different densities. Based on this simplification, weakly and strongly nonlinear models were established in various asymptotic limits, including, among others, the Korteweg-de Vries (KdV) equation and its variants, the Benjamin-Ono (BO) equation, and the Mayata-Choi-Camassa (MCC)

Figure 1   **a** Vertical profile of potential density (kg/m^3) measured at 21°55.8′N, 117°9.6′E, the South China Sea, on 20 May 2001. **b**, **c** Observed typical temperature (°C) profiles representing mode-2 convex and concave internal solitary waves, respectively. Figures are quoted from Ref. [3].

equations (the interested readers are referred to Refs. [4-6] for more details). These celebrated model equations provide powerful tools to explain field observations and physical mechanisms of the generation, propagation, and dissipation of internal waves.

While various nonlinear dispersive models for the two-fluid system have been successful in many aspects of internal wave problems, with the further development of field observations, the original physical assumptions and theoretical models show disadvantages. Perhaps, one of the biggest problems is that ignoring the thickness of the pycnocline results in the first baroclinic mode (mode-1) of internal waves only. However, other modes also exist in the ocean and, particularly, physical oceanographers recently have made extensive field observations on the second baroclinic mode (mode-2) internal waves in a number of places, including the South China Sea [7], the Andaman Sea of the Indian Ocean [8], the northern Heng-Chun Ridge [9], and the New Jersey Coast [10]. These mode-2 waves can be categorized into concave and convex types according to morphologically opposite directions of isotherm displacements (see Figs. 1b and c). In reality, the bathythermograph information indicates that the oceans display a basic three-layered structure akin to a sandwich in many places; see a typical ocean density profile in Fig. 1a. Considering the thickness of the middle layer can help to understand the higher-order modes of internal waves.

Experimental investigations on mode-2 internal waves are also being carried out intensively. In laboratories, these waves are generated by using the "gravitational collapse" method for three homogeneous fluids of different densities (see Ref. [11] for details). Based on the same technique,

experimentalists conducted further researches on mode-2 internal solitary-like waves to understand the effects of bottom topography on their propagations [12, 13] and their capability for mass transport [14]. On the theoretical side, to explain these experimental results, we need to develop three-layer weakly/strongly nonlinear dispersive models. As an added benefit, three-layer models with two sharp interfaces can be used to study internal waves when mode-1 and mode-2 components co-exist. This situation frequently occurs, for example, energy exchanges between mode-1 and mode-2 waves through bottom topography [15-18]. Another example is that the propagation of mode-2 solitary waves is usually accompanied by the tail of mode-1 waves [19], which has been verified theoretically by Akylas and Grimshaw [20] and numerically by Vanden-Broeck and Turner [21].

Recently, Barros et al. [22] extended the two-layer MCC model to three homogeneous layers confined between two flat and rigid boundaries to study strongly nonlinear mode-2 solitary waves. Their model assumes that internal waves characterized by deformations of two sharp interfaces are long compared to the total depth of fluids. However, in many cases, the bottom layer in the ocean is longer than internal waves, and hence model equations accounting for this situation need to be developed. In the present paper, we attempt to derive novel strongly/weakly nonlinear asymptotic models for the three-layer problem, where some layers are shallow, and the others are deep, compared with the characteristic wavelength.

The rest of the paper is structured as follows. The mathematical description and the Ablowitz-Fokas-Musslimani formulation of the problem are given in Sect. 2. For the hori-

zontally two-dimensional problem, strongly and weakly nonlinear model equations in the "shallow-shallow-deep" and "deep-shallow-deep" scenarios are derived in Sects. 3 and 4, respectively. The equations derived here are based on systematic asymptotic expansions of the global integrals related to the kinematic boundary conditions for different wavelength and amplitude scales. In addition, solitary waves are numerically computed in spatially one-dimensional models using the Petviashvili and Newton iterative methods. The corresponding global bifurcation diagrams are explored by a numerical continuation method. Finally, a conclusion is given in Sect. 5.

2.　Mathematical formulation

2.1　Governing equations

Consider a three-dimensional incompressible and inviscid fluid system, composed of three immiscible and homogeneous layers with adjacent layers separated by a sharp interface (see Fig. 2 for a schematic of the problem). The Cartesian coordinate system (x, y, z) is introduced such that the gravity is directed into the negative z-axis. The top and bottom layers are bounded by flat rigid lids located at $z = h_1$ and $z = -(h_2 + h_3)$, respectively, and the middle layer locates between two sharp interfaces $-h_2 + \eta_2(x, y, t) < z < \eta_1(x, y, t)$. The fluid density in each layer is supposed to be constant, designated by ρ_i ($i = 1, 2, 3$), and the system is in a stable configuration, namely $\rho_1 < \rho_2 < \rho_3$. The flow is assumed to be irrotational in each layer, indicating that there exists a potential function ϕ_i so that the velocity field can be expressed as its gradient. Finally, the conservation of mass implies that the velocity potential in each layer satisfies the Laplace
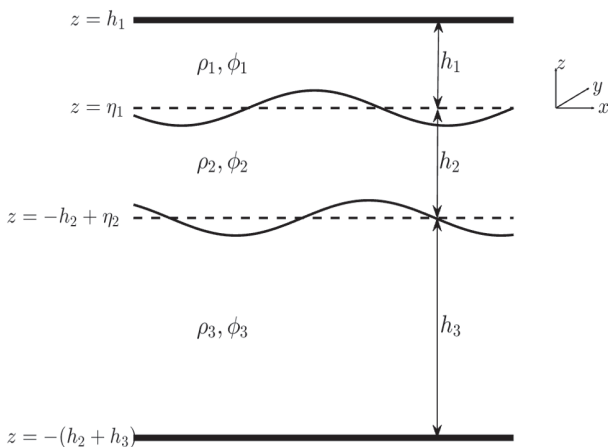
Figure 2　Mathematical idealization of the problem.

equation:

$$\phi_{ixx} + \phi_{iyy} + \phi_{izz} = 0, \qquad \text{for } i = 1, 2, 3. \tag{1}$$

At the upper interface $z = \eta_1(x, y, t)$, the nonlinear kinematic and dynamic boundary conditions read

$$\eta_{1t} = \phi_{1z} - \nabla \eta_1 \cdot \nabla \phi_1 = \phi_{2z} - \nabla \eta_1 \cdot \nabla \phi_2, \tag{2}$$

$$\rho_2 \left[\phi_{2t} + \frac{|\nabla \phi_2|^2}{2} + \frac{1}{2}(\phi_{2z})^2 + g\eta_1 \right]$$
$$= \rho_1 \left[\phi_{1t} + \frac{|\nabla \phi_1|^2}{2} + \frac{1}{2}(\phi_{1z})^2 + g\eta_1 \right], \tag{3}$$

where ∇ is the horizontal gradient operator and g is the acceleration due to gravity. Similarly, the kinematic and dynamic boundary conditions at the lower interface $z = -h_2 + \eta_2(x, y, t)$ can be expressed as

$$\eta_{2t} = \phi_{2z} - \nabla \eta_2 \cdot \nabla \phi_2 = \phi_{3z} - \nabla \eta_2 \cdot \nabla \phi_3, \tag{4}$$

$$\rho_3 \left[\phi_{3t} + \frac{|\nabla \phi_3|^2}{2} + \frac{1}{2}(\phi_{3z})^2 + g\eta_2 \right]$$
$$= \rho_2 \left[\phi_{2t} + \frac{|\nabla \phi_2|^2}{2} + \frac{1}{2}(\phi_{2z})^2 + g\eta_2 \right]. \tag{5}$$

At two rigid lids, the impermeability boundary conditions

$$\phi_{1z} = 0, \qquad \text{at } z = h_1, \tag{6}$$

$$\phi_{3z} = 0, \qquad \text{at } z = -(h_2 + h_3) \tag{7}$$

hold, which complete the mathematical description of the whole system.

2.2　Ablowitz-Fokas-Musslimani formulation

Recently, Ablowitz et al. [23] proposed an explicit non-local formulation for the classical water-wave problem in two and three dimensions. It was later generalized to study interfacial waves with a free surface [24] and with a variable bottom topography [25]. First of all, it is straightforward to verify that the following identity

$$(\phi_{iz}\psi_x + \phi_{ix}\psi_z)_x + (\phi_{iz}\psi_y + \phi_{iy}\psi_z)_y + (\phi_{iz}\psi_z - \nabla\phi_i \cdot \nabla\psi)_z = 0, \tag{8}$$

holds for an arbitrary harmonic function ψ. Applying the divergent theorem to Eq. (8) in the top layer yields

$$\int \{ [\eta_{1x}(\phi_{1z}\psi_x + \phi_{1x}\psi_z) + \eta_{1y}(\phi_{1z}\psi_y + \phi_{1y}\psi_z)$$
$$- (\phi_{1z}\psi_z - \nabla\phi_1 \cdot \nabla\psi)]_{z=\eta_1} - \nabla\phi_1 \cdot \nabla\psi|_{z=h_1} \} d\mathbf{r} = 0, \tag{9}$$

where $\mathbf{r} = (x, y)$ is a vector in the horizontal plane. Substituting $\psi = e^{i\mathbf{k}\cdot\mathbf{r} + |\mathbf{k}|z}$ into Eq. (9) yields

$$\int e^{i\mathbf{k}\cdot\mathbf{r}} [(-|\mathbf{k}|\eta_{1t} + i\mathbf{k} \cdot \nabla\Phi_1^-) e^{|\mathbf{k}|(\eta_1 - h_1)}$$
$$- i\mathbf{k} \cdot \nabla\phi_1|_{z=h_1}] d\mathbf{r} = 0, \tag{10}$$

where $\mathbf{k} = (k_x, k_y)$ is the wavenumber vector, $|\mathbf{k}| = \sqrt{k_x^2 + k_y^2}$ is the corresponding magnitude, and Φ_1^- is defined as $\Phi_1^- = \phi_1(x, y, \eta_1(x, y, t), t)$. Since $\psi = \mathrm{e}^{\mathrm{i}\mathbf{k}\cdot\mathbf{r} - |\mathbf{k}|z}$ is also a solution to the Laplace equation, one then obtains

$$\int \mathrm{e}^{\mathrm{i}\mathbf{k}\cdot\mathbf{r}} \Big[(|\mathbf{k}|\eta_{1t} + \mathrm{i}\mathbf{k}\cdot\nabla\Phi_1^-)\,\mathrm{e}^{-|\mathbf{k}|(\eta_1 - h_1)}$$
$$- \mathrm{i}\mathbf{k}\cdot\nabla\phi_1\big|_{z=h_1} \Big]\mathrm{d}\mathbf{r} = 0. \tag{11}$$

Subtracting Eq. (10) from Eq. (11) gives

$$\int \mathrm{e}^{\mathrm{i}\mathbf{k}\cdot\mathbf{r}} \Big[\eta_{1t} \cosh(|\mathbf{k}|(h_1 - \eta_1))$$
$$+ \mathrm{i}\mathbf{k}\cdot\nabla\Phi_1^- \frac{\sinh(|\mathbf{k}|(h_1 - \eta_1))}{|\mathbf{k}|} \Big]\mathrm{d}\mathbf{r} = 0. \tag{12}$$

In the same vein, one can obtain the global relations for the middle layer

$$\int \mathrm{e}^{\mathrm{i}\mathbf{k}\cdot\mathbf{r} + |\mathbf{k}|(-h_2 + \eta_2)} \big(- |\mathbf{k}|\eta_{2t} + \mathrm{i}\mathbf{k}\cdot\nabla\Phi_2^- \big)\mathrm{d}\mathbf{r}$$
$$+ \int \mathrm{e}^{\mathrm{i}\mathbf{k}\cdot\mathbf{r} + |\mathbf{k}|\eta_1} (|\mathbf{k}|\eta_{1t} - \mathrm{i}\mathbf{k}\cdot\nabla\Phi_2^+)\mathrm{d}\mathbf{r} = 0, \tag{13}$$

and

$$\int \mathrm{e}^{\mathrm{i}\mathbf{k}\cdot\mathbf{r} - |\mathbf{k}|(-h_2 + \eta_2)} (|\mathbf{k}|\eta_{2t} + \mathrm{i}\mathbf{k}\cdot\nabla\Phi_2^-)\mathrm{d}\mathbf{r}$$
$$+ \int \mathrm{e}^{\mathrm{i}\mathbf{k}\cdot\mathbf{r} - |\mathbf{k}|\eta_1} \big(- |\mathbf{k}|\eta_{1t} - \mathrm{i}\mathbf{k}\cdot\nabla\Phi_2^+ \big)\mathrm{d}\mathbf{r} = 0, \tag{14}$$

where $\Phi_2^{\pm}$ are defined as

$$\Phi_2^- = \phi_2(x, y, -h_2 + \eta_2(x, y, t), t), \quad \Phi_2^+ = \phi_2(x, y, \eta_1(x, y, t), t).$$

It follows directly from adding and subtracting Eqs. (13) and (14) that

$$\int \mathrm{e}^{\mathrm{i}\mathbf{k}\cdot\mathbf{r}} [|\mathbf{k}|\sinh(|\mathbf{k}|(h_2 - \eta_2))\eta_{2t} + \mathrm{i}\mathbf{k}\cdot\nabla\Phi_2^- \cosh(|\mathbf{k}|(h_2 - \eta_2))$$
$$+ |\mathbf{k}|\sinh(|\mathbf{k}|\eta_1)\eta_{1t} - \mathrm{i}\mathbf{k}\cdot\nabla\Phi_2^+ \cosh(|\mathbf{k}|\eta_1)]\mathrm{d}\mathbf{r} = 0, \tag{15}$$

and

$$\int \mathrm{e}^{\mathrm{i}\mathbf{k}\cdot\mathbf{r}} \Big[- \cosh(|\mathbf{k}|(h_2 - \eta_2))\eta_{2t} - \mathrm{i}\mathbf{k}\cdot\nabla\Phi_2^- \frac{\sinh(|\mathbf{k}|(h_2 - \eta_2))}{|\mathbf{k}|}$$
$$+ \cosh(|\mathbf{k}|\eta_1)\eta_{1t} - \mathrm{i}\mathbf{k}\cdot\nabla\Phi_2^+ \frac{\sinh(|\mathbf{k}|\eta_1)}{|\mathbf{k}|} \Big]\mathrm{d}\mathbf{r} = 0. \tag{16}$$

Substituting $\psi = \mathrm{e}^{\mathrm{i}\mathbf{k}\cdot\mathbf{r} \pm |\mathbf{k}|(z + h_2 + h_3)}$ into the global relation for the bottom layer yields

$$\int \mathrm{e}^{\mathrm{i}\mathbf{k}\cdot\mathbf{r}} [\mathrm{i}\mathbf{k}\cdot\nabla\phi_3\big|_{z=-(h_2 + h_3)}$$
$$+ \mathrm{e}^{|\mathbf{k}|(h_3 + \eta_2)} \big(-\mathrm{i}\mathbf{k}\cdot\nabla\Phi_3^+ + |\mathbf{k}|\eta_{2t} \big)]\mathrm{d}\mathbf{r} = 0, \tag{17}$$

and

$$\int \mathrm{e}^{\mathrm{i}\mathbf{k}\cdot\mathbf{r}} [\mathrm{i}\mathbf{k}\cdot\nabla\phi_3\big|_{z=-(h_2 + h_3)}$$

$$+ \mathrm{e}^{-|\mathbf{k}|(h_3 + \eta_2)} (-\mathrm{i}\mathbf{k}\cdot\nabla\Phi_3^+ - |\mathbf{k}|\eta_{2t})]\mathrm{d}\mathbf{r} = 0, \tag{18}$$

where $\Phi_3^+ = \phi_3(x, y, -h_2 + \eta_2(x, y, t), t)$. Subtracting Eq. (18) from Eq. (17) gives

$$\int \mathrm{e}^{\mathrm{i}\mathbf{k}\cdot\mathbf{r}} \Big[\cosh(|\mathbf{k}|(h_3 + \eta_2))\eta_{2t}$$
$$- \mathrm{i}\mathbf{k}\cdot\nabla\Phi_3^+ \frac{\sinh(|\mathbf{k}|(h_3 + \eta_2))}{|\mathbf{k}|} \Big]\mathrm{d}\mathbf{r} = 0. \tag{19}$$

Next, we rewrite the dynamic boundary conditions using the interfacial variables. At $z = \eta_1(x, y, t)$, the time evolution of $\rho_2\Phi_2^+ - \rho_1\Phi_1^-$ satisfies

$$(\rho_2\Phi_2^+ - \rho_1\Phi_1^-)_t + g(\rho_2 - \rho_1)\eta_1$$
$$+ \frac{\rho_2}{2}\Big[- \frac{(\eta_{1t} + \nabla\eta_1 \cdot \nabla\Phi_2^+)^2}{1 + |\nabla\eta_1|^2} + |\nabla\Phi_2^+|^2 \Big]$$
$$- \frac{\rho_1}{2}\Big[|\nabla\Phi_1^-|^2 - \frac{(\eta_{1t} + \nabla\eta_1 \cdot \nabla\Phi_1^-)^2}{1 + |\nabla\eta_1|^2} \Big] = 0, \tag{20}$$

while at $z = -h_2 + \eta_2(x, y, t)$, the governing equation for $\rho_3\Phi_3^+ - \rho_2\Phi_2^-$ reads

$$(\rho_3\Phi_3^+ - \rho_2\Phi_2^-)_t + g(\rho_3 - \rho_2)\eta_2$$
$$+ \frac{\rho_3}{2}\Big[\frac{-(\eta_{2t} + \nabla\eta_2 \cdot \nabla\Phi_3^+)^2}{1 + |\nabla\eta_2|^2} + |\nabla\Phi_3^+|^2 \Big]$$
$$- \frac{\rho_2}{2}\Big[|\nabla\Phi_2^-|^2 - \frac{(\eta_{2t} + \nabla\eta_2 \cdot \nabla\Phi_2^-)^2}{1 + |\nabla\eta_2|^2} \Big] = 0. \tag{21}$$

3.   Shallow-shallow-deep scenario

3.1   Strongly nonlinear models

In the two-layer system, when the thickness of the upper fluid layer is small compared with the characteristic wavelength and the lower layer is of great depth (which is termed the "shallow-deep" case hereafter), weakly nonlinear models were derived in Ref. [4] for two horizontal dimensions and the strongly nonlinear model was derived in Ref. [5] for the horizontally one-dimensional case. In the subsequent analyses for deriving a novel strongly nonlinear model, the generalization of Ref. [5] is twofold: three-layer configuration and two horizontal dimensions. We assume the top and middle layers are thin and the bottom layer is thick, compared to the typical wavelength of interfaces. We call this configuration the "shallow-shallow-deep" case. To continue the derivation, the following scales

$$x, y, h_3 \sim \lambda, \ \eta_{1,2} \sim h_2, \ t \sim \frac{\lambda}{c_0}, \ \Phi_{1,2,3}^{\pm} \sim \lambda c_0, \ h_1 \sim h_2$$

are used, where c_0 is the characteristic speed, λ is the typical wavelength, and no assumption is made on wave amplitude.

We denote by $\mu = \frac{h_2}{\lambda}$ the small parameter measuring the ratio of middle layer thickness to typical wavelength. After non-dimensionalization, the global relations Eqs. (12), (15), (16), and (19) become

$$\int e^{i\mathbf{k}\cdot\mathbf{r}}\left[\cosh(\mu|\mathbf{k}|(h_1 - \eta_1))\eta_{1t}\right.$$
$$+ i\mathbf{k}\cdot\nabla\Phi_1^- \frac{\sinh(\mu|\mathbf{k}|(h_1 - \eta_1))}{\mu|\mathbf{k}|}\Big]d\mathbf{r} = 0\,, \tag{22}$$

$$\int e^{i\mathbf{k}\cdot\mathbf{r}}[\mu|\mathbf{k}|\sinh(\mu|\mathbf{k}|(1 - \eta_2))\eta_{2t}$$
$$+ i\mathbf{k}\cdot\nabla\Phi_2^- \cosh(\mu|\mathbf{k}|(1 - \eta_2))$$
$$+ \mu|\mathbf{k}|\sinh(\mu|\mathbf{k}|\eta_1)\eta_{1t}$$
$$- i\mathbf{k}\cdot\nabla\Phi_2^+ \cosh(\mu|\mathbf{k}|\eta_1)]d\mathbf{r} = 0\,, \tag{23}$$

$$\int e^{i\mathbf{k}\cdot\mathbf{r}}\left[-\cosh(\mu|\mathbf{k}|(1 - \eta_2))\eta_{2t}\right.$$
$$- i\mathbf{k}\cdot\nabla\Phi_2^- \frac{\sinh(\mu|\mathbf{k}|(1 - \eta_2))}{\mu|\mathbf{k}|} + \cosh(\mu|\mathbf{k}|\eta_1)\eta_{1t}$$
$$- i\mathbf{k}\cdot\nabla\Phi_2^+ \frac{\sinh(\mu|\mathbf{k}|\eta_1)}{\mu|\mathbf{k}|}\Big]d\mathbf{r} = 0\,, \tag{24}$$

and

$$\int e^{i\mathbf{k}\cdot\mathbf{r}}\left[\mu\eta_{2t} - i\mathbf{k}\cdot\nabla\Phi_3^+ \frac{\tanh(|\mathbf{k}|(h_3 + \mu\eta_2))}{|\mathbf{k}|}\right]d\mathbf{r} = 0\,, \tag{25}$$

where we follow the original variables for ease of notation. Expanding the global relations Eqs. (22)-(25) about the small parameter μ and retaining terms valid up to $O(\mu)$, one obtains

$$\int e^{i\mathbf{k}\cdot\mathbf{r}}\left[\eta_{1t} + i\mathbf{k}\cdot\nabla\Phi_1^-(h_1 - \eta_1)\right]d\mathbf{r} = 0\,, \tag{26}$$

$$\int e^{i\mathbf{k}\cdot\mathbf{r}}\left(i\mathbf{k}\cdot\nabla\Phi_2^- - i\mathbf{k}\cdot\nabla\Phi_2^+\right)d\mathbf{r} = 0\,, \tag{27}$$

$$\int e^{i\mathbf{k}\cdot\mathbf{r}}[-\eta_{2t} - i\mathbf{k}\cdot\nabla\Phi_2^-(1 - \eta_2)$$
$$+ \eta_{1t} - i\mathbf{k}\cdot\nabla\Phi_2^+\eta_1]d\mathbf{r} = 0\,, \tag{28}$$

and

$$\int e^{i\mathbf{k}\cdot\mathbf{r}}\left\{\mu\eta_{2t} - i\mathbf{k}\cdot\nabla\Phi_3^+\left[\frac{\tanh(|\mathbf{k}|h_3)}{|\mathbf{k}|} + \mu\eta_2\right.\right.$$
$$- \mu\tanh^2(|\mathbf{k}|h_3)\eta_2\Big]\Big\}d\mathbf{r} = 0\,. \tag{29}$$

Upon noting $i\mathbf{k} \sim -\nabla$ and $k^2 \sim -\Delta$, we take the inverse Fourier transforms of Eqs. (26)-(29), which yield

$$\eta_{1t} - h_1\Delta\Phi_1^- + \nabla\cdot\eta_1\nabla\Phi_1^- = 0\,, \tag{30}$$

$$\Phi_2^- = \Phi_2^+\,, \tag{31}$$

$$\eta_{1t} - \eta_{2t} + \Delta\Phi_2^- - \nabla\cdot\eta_2\nabla\Phi_2^- + \nabla\cdot\eta_1\nabla\Phi_2^+ = 0\,, \tag{32}$$

$$\Phi_3^+ = \mu G_3^{-1}\eta_{2t} + O\left(\mu^2\right)\,, \tag{33}$$

where G_3 is a pseudo-differential operator with the Fourier symbol

$$\widehat{G_3} = |\mathbf{k}|\tanh\left(|\mathbf{k}|h_3\right)\,, \tag{34}$$

where $h_3 = O(1)$ or even larger. On the other hand, with the dimensionless variables, the dynamic boundary conditions read

$$(\rho_2\Phi_2^+ - \rho_1\Phi_1^-)_t + \frac{gh_2(\rho_2 - \rho_1)}{c_0^2}\eta_1 + \frac{\rho_2}{2}\left[|\nabla\Phi_2^+|^2\right.$$
$$- \frac{\mu^2(\eta_{1t} + \nabla\eta_1\cdot\nabla\Phi_2^+)^2}{1 + \mu^2|\nabla\eta_1|^2}\Big] - \frac{\rho_1}{2}\left[|\nabla\Phi_1^-|^2\right.$$
$$- \frac{\mu^2(\eta_{1t} + \nabla\eta_1\cdot\nabla\Phi_1^-)^2}{1 + \mu^2|\nabla\eta_1|^2}\Big] = 0\,, \tag{35}$$

and

$$(\rho_3\Phi_3^+ - \rho_2\Phi_2^-)_t + \frac{gh_2(\rho_3 - \rho_2)}{c_0^2}\eta_2 + \frac{\rho_3}{2}\left[|\nabla\Phi_3^+|^2\right.$$
$$- \frac{\mu^2(\eta_{2t} + \nabla\eta_2\cdot\nabla\Phi_3^+)^2}{1 + \mu^2|\nabla\eta_2|^2}\Big] - \frac{\rho_2}{2}\left[|\nabla\Phi_2^-|^2\right.$$
$$- \frac{\mu^2(\eta_{2t} + \nabla\eta_2\cdot\nabla\Phi_2^-)^2}{1 + \mu^2|\nabla\eta_2|^2}\Big] = 0\,, \tag{36}$$

where the characteristic speed c_0 can be defined as

$$c_0 = \sqrt{\frac{gh_2(\rho_3 - \rho_1)}{\rho_2}}\,.$$

Since the difference between Φ_2^- and Φ_2^+ is $O\left(\mu^2\right)$, which will not be involved in the reduced model, we can suppress the superscript of Φ_1^-, $\Phi_2^\pm$ and Φ_3^+ for simplicity. Substituting Eq. (33) into Eq. (36) and retaining terms valid up to $O(\mu)$, Eq. (36) can be rewritten as

$$\Phi_{2t} - \frac{R_3 - 1}{R_3 - R_1}\eta_2 + \frac{1}{2}|\nabla\Phi_2|^2 - \mu R_3 G_3^{-1}\eta_{2tt} = 0\,, \tag{37}$$

where $R_1 = \frac{\rho_1}{\rho_2} < 1$ and $R_3 = \frac{\rho_3}{\rho_2} > 1$. Using Eq. (37) to eliminate Φ_{2t} in Eq. (35), one obtains

$$\Phi_{1t} - \frac{1 - R_1}{R_1(R_3 - R_1)}\eta_1 - \frac{R_3 - 1}{R_1(R_3 - R_1)}\eta_2$$
$$+ \frac{1}{2}|\nabla\Phi_1|^2 - \frac{\mu R_3}{R_1}G_3^{-1}\eta_{2tt} = 0\,. \tag{38}$$

Finally, Eqs. (30) and (32) can be recast to

$$\eta_{1t} - h_1\Delta\Phi_1 + \nabla\cdot\eta_1\nabla\Phi_1 = 0\,, \tag{39}$$

$$\eta_{2t} - h_1\Delta\Phi_1 - \Delta\Phi_2 + \nabla\cdot\eta_1\nabla\Phi_1$$
$$+ \nabla\cdot(\eta_2 - \eta_1)\nabla\Phi_2 = 0\,. \tag{40}$$

Equations (37)-(40) form a closed system for four unknowns $\Phi_{1,2}$ and $\eta_{1,2}$, a fully nonlinear weakly dispersive model. This model generalizes the Miyata-Choi-Camassa equations proposed in Ref. [5] to the three-fluid system and horizontally two-dimensional situation (this fact becomes apparent if we

use $\mathbf{u}_{1,2} = \nabla \Phi_{1,2}$ and $\eta_{1,2}$ as unknowns). We finally remark that if the problem is y-independent and the bottom layer is infinitely deep, the system Eqs. (37)-(40) reduces to

$$
\begin{cases}
\eta_{1t} - [(h_1 - \eta_1)u_1]_x = 0, \\
\eta_{2t} - [(h_1 - \eta_1)u_1]_x - [(1 + \eta_1 - \eta_2)u_2]_x = 0, \\
u_{1t} - \dfrac{1 - R_1}{R_1(R_3 - R_1)}\eta_{1x} - \dfrac{R_3 - 1}{R_1(R_3 - R_1)}\eta_{2x} + u_1 u_{1x} \\
\quad = \dfrac{\mu R_3}{R_1}\mathscr{H}[(h_1 - \eta_1)u_1 + (1 + \eta_1 - \eta_2)u_2]_{xt}, \\
u_{2t} - \dfrac{R_3 - 1}{R_3 - R_1}\eta_{2x} + u_2 u_{2x} \\
\quad = \mu R_3 \mathscr{H}[(h_1 - \eta_1)u_1 + (1 + \eta_1 - \eta_2)u_2]_{xt},
\end{cases} \tag{41}
$$

where $\mathscr{H}$ is the Hilbert transform with the Fourier symbol $\mathrm{isgn}(k)$.

3.2 Weakly nonlinear models

To derive weakly nonlinear models, we assume a small-amplitude motion in addition to the long-wave assumption, then choose the following scales

$$
x, y, h_3 \sim \lambda, \quad h_1 \sim h_2, \quad \eta_{1,2} \sim a,
$$
$$
k_x, k_y \sim \frac{1}{\lambda}, \quad t \sim \frac{\lambda}{c_0}, \quad \Phi_i^{\pm} \sim \frac{a\lambda}{h_2}c_0,
$$

where a is the characteristic scale of wave amplitude, and other quantities are the same as the strongly nonlinear model. Two small parameters, $\mu = \frac{h_2}{\lambda}$ and $\epsilon = \frac{a}{h_2}$, are introduced to measure the dispersive and nonlinear effects, respectively. To continue the derivation, we follow the same procedure as Sect. 3.1:

• Non-dimensionalizing the global relations and dynamic boundary conditions;

• Expanding these expressions about the small parameters μ and ϵ;

• Retaining terms valid up to $O(\mu, \epsilon)$ where $\mu \sim \epsilon$ for balancing dispersion and nonlinearity.

After a tedious calculation, one finally arrives at

$$
\eta_{1t} - h_1 \Delta \Phi_1 + \epsilon \nabla \cdot \eta_1 \nabla \Phi_1 = 0, \tag{42}
$$

$$
\eta_{2t} - h_1 \Delta \Phi_1 - \Delta \Phi_2 + \epsilon \nabla \cdot \eta_1 \nabla \Phi_1
$$
$$
+ \epsilon \nabla \cdot (\eta_2 - \eta_1) \nabla \Phi_2 = 0, \tag{43}
$$

$$
\Phi_{1t} - \frac{1 - R_1}{R_1(R_3 - R_1)}\eta_1 - \frac{R_3 - 1}{R_1(R_3 - R_1)}\eta_2 + \frac{\epsilon}{2}|\nabla \Phi_1|^2
$$
$$
- \frac{\mu R_3}{R_1}G_3^{-1}\eta_{2tt} = 0, \tag{44}
$$

$$
\Phi_{2t} - \frac{R_3 - 1}{R_3 - R_1}\eta_2 + \frac{\epsilon}{2}|\nabla \Phi_2|^2 - \mu R_3 G_3^{-1}\eta_{2tt} = 0. \tag{45}
$$

Equations (42)-(45) form a Boussinesq type model. We can further reduce the number of equations to two by eliminating

$\eta_{1,2}$. For this purpose, we take the derivative of Eqs. (44) and (45) with respect to t and then eliminate η_{1t} and η_{2t} using Eqs. (42) and (43). Finally, replacing η_1 with $\frac{R_1}{D}\Phi_{1t} - \frac{\Phi_{2t}}{D}$ and η_2 with $\frac{\Phi_{2t}}{1-D}$ where $D = \frac{1 - R_1}{R_3 - R_1}$, one obtains

$$
0 = \Phi_{1tt} - \frac{h_1}{R_1}\Delta \Phi_1 - \frac{1 - D}{R_1}\Delta \Phi_2
$$
$$
- \frac{\mu R_3}{R_1}G_3^{-1}\Delta(h_1 \Phi_1 + \Phi_2)_{tt} + \epsilon \left(|\nabla \Phi_1|_t^2 + \Phi_{1t}\Delta \Phi_1\right)
$$
$$
+ \frac{\epsilon}{D}\nabla \cdot \left[(1 - D)\Phi_{1t} - \frac{1}{R_1}\Phi_{2t}\right]\nabla(\Phi_1 - \Phi_2), \tag{46}
$$

and

$$
0 = \Phi_{2tt} - h_1(1 - D)\Delta \Phi_1 - (1 - D)\Delta \Phi_2
$$
$$
- \mu R_3 G_3^{-1}\Delta(h_1 \Phi_1 + \Phi_2)_{tt} + \epsilon \left(|\nabla \Phi_2|_t^2 + \Phi_{2t}\Delta \Phi_2\right)
$$
$$
+ \frac{\epsilon(1 - D)}{D}\nabla \cdot (R_1 \Phi_{1t} - \Phi_{2t})\nabla(\Phi_1 - \Phi_2). \tag{47}
$$

Equations (46) and (47) form a closed system for two unknowns $\Phi_{1,2}$, It is noted that Eqs. (46) and (47) are derived based on the Benjamin-Ono scaling, with the Benney-Luke type nonlinearities, hence termed the Benjamin-Ono-Benney-Luke system hereafter.

3.3 Results

In the following subsections, we focus on the numerical computation of solitary waves, a type of traveling-wave solutions decaying in the direction of propagation. We confine ourselves to the horizontally one-dimensional situation in the "shallow-shallow-deep" models and send h_3 to infinity for simplicity. Both strongly and weakly nonlinear models will be calculated and compared with each other.

3.3.1 Dispersion relation

Before computing solitary waves, we derive the linear dispersion relation of the problem, which can predict the speed range of solitary waves. Whether the strongly nonlinear model (Eqs. (37)-(40)) or weakly nonlinear model (Eqs. (42)-(45)) is used for the "shallow-shallow-deep" case, the linearized system is the same. Solutions to the linearized equations are sought as being proportional to $\mathrm{e}^{ik(x-ct)}$, with the wavenumber k and phase speed c; namely, we write $\eta_{1,2} = \widehat{\eta}_{1,2}\mathrm{e}^{ik(x-ct)}$ and $\Phi_{1,2} = \widehat{\Phi}_{1,2}\mathrm{e}^{ik(x-ct)}$. The linearized system for $\widehat{\eta}_{1,2}$ and $\widehat{\Phi}_{1,2}$ is homogeneous, and the existence of non-trivial solutions indicates the relation between c and k, which satisfies

$$
[R_1 + \mu R_3(h_1 + R_1)|k|]c^4 - [(1 - D)R_1
$$
$$
+ h_1 + \mu h_1 R_3 D|k|]c^2 + D(1 - D)h_1 = 0. \tag{48}
$$

It is not difficult to verify that the four roots of Eq. (48) are all real and can be divided into two categories according to

the magnitude. The phase speed is termed mode-1 for larger magnitude and mode-2 for smaller magnitude. In the long-wave limit ($k \to 0$), the linear phase speeds $c_0^\pm$ read

$$(c_0^\pm)^2 = \frac{(1-D)R_1 + h_1}{2R_1}$$
$$\pm \frac{\sqrt{[(1-D)R_1 - h_1]^2 + 4R_1 h_1 (1-D)^2}}{2R_1}, \tag{49}$$

while for the short-wave limit ($k \to \infty$),

$$c_\infty^- = 0, \qquad (c_\infty^+)^2 = \frac{Dh_1}{R_1 + h_1}, \tag{50}$$

where superscripts "+" and "-" refer to mode-1 and mode-2, respectively. A straightforward calculation shows that $c_\infty^+ \geq c_0^-$, and the equality holds if and only if $D = 0$.

Figure 3 shows the dispersion relation of the "shallow-shallow-deep" case for $R_1 = 0.5$, $R_3 = 1.3$, and $h_1 = 5$. Note that only the positive roots to Eq. (48) are plotted, and both mode-1 (solid line) and mode-2 (dashed line) curves are monotonically decreasing functions of wavenumber. Since c_0^+ is finite and $c_\infty^+ > c_0^-$, it can be inferred from the linear dispersion relation that solitary waves may bifurcate from $c_0^\pm$ and exist for $c > c_0^+$ and $c_0^- < c < c_\infty^+$, where c is the translating speed of a solitary wave. We next show that the terminologies, mode-1 and mode-2, are also rational for solitary waves. The linearized system implies

$$\frac{\widehat{\eta_1}}{\widehat{\eta_2}} = 1 - \frac{1-D}{c^2}. \tag{51}$$

The two interfaces are locked in-phase at $c = c_0^+$ since $\widehat{\eta_1}/\widehat{\eta_2} > 0$ due to the explicit expression Eq. (49). On the other hand, it is not difficult to show that $\widehat{\eta_1}/\widehat{\eta_2} < 0$ at $c = c_0^-$,
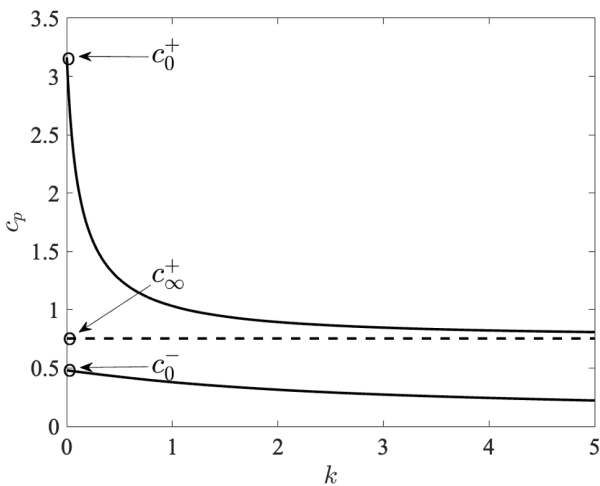
Figure 3 Dispersion relation Eq. (48) for $R_1 = 0.5$, $R_3 = 1.3$, and $h_1 = 5$: solid line, mode-1 branch; dashed line, mode-2 branch. Critical points are labeled by circles: $c_0^+ = 3.1850$, $c_0^- = 0.4807$, and $c_\infty^+ = 0.7538$.

the two interfaces are out-of-phase. It is noted that a solution with the translating speed $c \in \left(c_0^-, c_\infty^+\right)$ is usually called the gap solitary wave in the literature.

3.3.2 Solitary waves

This section is intended to give internal solitary-wave solutions to strongly and weakly nonlinear models derived in Sects. 3.1 and 3.2, respectively. Both mode-1 and mode-2 solitary waves are shown to exist in these models. The weakly nonlinear model can be solved analytically with the aid of the famous Benjamin-Ono equation. While the strongly nonlinear model will be solved using the numerical method based on the Petviashvili iteration scheme.

We start with the weakly nonlinear model. A moving coordinate $\xi = x - ct$ is introduced such that the traveling wave propagating with the same velocity becomes static in the new frame of reference. The subsequent analyses show that the system Eqs. (42)-(45) can be asymptotically approximated by the steady Benjamin-Ono equation, which possesses a one-parameter family of solitons with algebraic decay. Firstly, in the moving frame, it can be inferred from Eqs. (42) and (44) that

$$\Phi_{1\xi} = -\frac{c}{h_1}\eta_1 - \frac{\epsilon c}{h_1^2}\eta_1^2 + O(\epsilon^2),$$

$$\Phi_{1\xi} = -\frac{D}{cR_1}\eta_1 - \frac{1-D}{cR_1}\eta_2 + \frac{\epsilon}{2c^3 R_1^2}[D\eta_1 + (1-D)\eta_2]^2$$
$$- \frac{\mu c R_3}{R_1}\mathscr{H}\left[\eta_{2\xi}\right] + O(\epsilon^2),$$

based on the equivalent substitution. Subtracting one equation from the other to eliminate $\Phi_{1\xi}$, one can express η_1 in terms of η_2, valid up to $O(\epsilon, \mu)$, as

$$\eta_1 = \frac{(1-D)h_1}{c^2 R_1 - Dh_1}\eta_2 - \frac{3\epsilon(1-D)^2 c^2 R_1 h_1}{2(c^2 R_1 - Dh_1)^3}\eta_2^2$$
$$+ \frac{\mu c^2 R_3 h_1}{c^2 R_1 - Dh_1}\mathscr{H}[\eta_{2\xi}] + O(\epsilon^2). \tag{52}$$

In the same vein, Eqs. (43) and (45) can be rewritten as

$$\Phi_{2\xi} = c\left(\eta_1 - \eta_2\right) - \epsilon c\left(\eta_1 - \eta_2\right)^2 + O(\epsilon^2),$$

$$\Phi_{2\xi} = -\frac{1-D}{c}\eta_2 + \frac{\epsilon(1-D)^2}{2c^3}\eta_2^2 - \mu c R_3 \mathscr{H}\left[\eta_{2\xi}\right] + O(\epsilon^2),$$

which can be used to establish another relation between η_1 and η_2 by eliminating $\Phi_{2\xi}$

$$\left[c^2 - (1-D)\right]\eta_2 - c^2\eta_1 + \epsilon\left[c^2(\eta_1 - \eta_2)^2\right.$$
$$\left. + \frac{(1-D)^2}{2c^2}\eta_2^2\right] - \mu c^2 R_3 \mathscr{H}\left[\eta_{2\xi}\right] + O(\epsilon^2) = 0. \tag{53}$$

Upon substituting Eq. (52) into Eq. (53) to cancel η_1 and retaining terms valid up to $O(\epsilon, \mu)$, one obtains the steady Benjamin-Ono equation in a moving frame

$$-\lambda\eta_2 + \frac{\alpha}{2}\eta_2^2 - \beta\mathcal{H}\left[\eta_{2\xi}\right] = 0\,, \tag{54}$$

where

$$
\begin{aligned}
\lambda =& (1 - D)\left(c^2 R_1 - Dh_1\right) - c^2\left(c^2 R_1 - h_1\right)\,, \\
\alpha =& \epsilon\left[\frac{3(1-D)^2 c^4 R_1 h_1}{\left(c^2 R_1 - Dh_1\right)^2} + \frac{(1-D)^2(c^2 R_1 - Dh_1)}{c^2}\right.\\
&\left. + \frac{2c^2(h_1 - c^2 R_1)^2}{c^2 R_1 - Dh_1}\right]\,, \\
\beta =& \mu c^2 R_3\left(c^2 h_1 + c^2 R_1 - Dh_1\right)\,.
\end{aligned}
$$

Eq. (54) was initially solved by Ono [26], who gave an analytical traveling-wave solution:

$$\eta_2(\xi) = \frac{a\delta^2}{\delta^2 + \xi^2}\,, \tag{55}$$

where $\lambda = \frac{a\alpha}{4}$ and $|\delta| = \frac{4\beta}{a\alpha}$. Then Eq. (55) provides an asymptotic solution to the weakly nonlinear model Eqs. (42)-(45) including leading- and next-to-leading-order approximations for both mode-1 and mode-2 solitary waves depending on the choice of c.

The numerical scheme for seeking solitary-wave solutions in the strongly nonlinear model Eq. (41) is a modification of the method initially proposed by Petviashvili [27], and the basic idea is to perform the fixed-point iteration in the Fourier space. For a fully localized traveling wave, the system (41) reads

$$
\begin{cases}
c\eta_1 + (h_1 - \eta_1)u_1 = 0\,, \\
c\eta_2 + (h_1 - \eta_1)u_1 + (1 + \eta_1 - \eta_2)u_2 = 0\,, \\
\frac{1}{2}u_1^2 - cu_1 - \frac{D}{R_1}\eta_1 - \frac{1-D}{R_1}\eta_2 \\
\quad + \frac{\mu c R_3}{R_1}\mathcal{H}[(h_1 - \eta_1)u_1 + (1 + \eta_1 - \eta_2)u_2]_\xi = 0\,, \\
\frac{1}{2}u_2^2 - cu_2 - (1 - D)\eta_2 + \mu c R_3\mathcal{H}[(h_1 - \eta_1)u_1 \\
\quad + (1 + \eta_1 - \eta_2)u_2]_\xi = 0\,,
\end{cases}
\tag{56}
$$

where the equations have been integrated with respect to ξ. Applying the Fourier transform to the system Eq. (56) and writing the system in the matrix form, one obtains

$$\widehat{\mathcal{L}_s}\,\widehat{\Lambda}_s = \widehat{\mathcal{N}_s[\Lambda_s]}\,, \tag{57}$$

where the hat symbol denotes the Fourier transform,

$$
\widehat{\mathcal{L}_s} = \begin{bmatrix}
-c & 0 & -h_1 & 0 \\
0 & -c & -h_1 & -1 \\
-\frac{D}{R_1} & -\frac{1-D}{R_1} & -c - \frac{ch_1 R_3}{R_1}|k|\mu & -\frac{cR_3}{R_1}|k|\mu \\
0 & -(1-D) & -ch_1 R_3|k|\mu & -c - cR_3|k|\mu
\end{bmatrix}\,,
$$

$$
\widehat{\Lambda}_s = \begin{bmatrix}
\widehat{\eta_1} \\
\widehat{\eta_2} \\
\widehat{u_1} \\
\widehat{u_2}
\end{bmatrix}\,,
$$

and

$$
\widehat{\mathcal{N}_s[\Lambda_s]} = \begin{bmatrix}
-\widehat{\eta_1 u_1} \\
\widehat{\eta_1 u_2} - \widehat{\eta_1 u_1} - \widehat{\eta_2 u_2} \\
-\frac{1}{2}\widehat{u_1^2} - \frac{\mu c R_3}{R_1}|k|\widehat{u_1 \eta_1} + \frac{\mu c R_3}{R_1}|k|u_2\widehat{(\eta_1 - \eta_2)} \\
-\frac{1}{2}\widehat{u_2^2} - \mu c R_3|k|\widehat{u_1 \eta_1} + \mu c R_3|k|u_2\widehat{(\eta_1 - \eta_2)}
\end{bmatrix}\,.
$$

We can then rewrite the system (56) as

$$\widehat{\Lambda}_s = \widehat{\mathcal{L}_s}^{-1}\widehat{\mathcal{N}_s[\Lambda_s]} = Q\left[\widehat{\Lambda}_s\right]\,, \tag{58}$$

where the operator Q is short for the combination of the linear and nonlinear operators. Since the Fourier transforms of the product terms in $\widehat{\mathcal{N}_s[\Lambda_s]}$ can be expressed as convolutions of $\widehat{\Lambda}_s$, we write Q as a function of $\widehat{\Lambda}_s$. Following Refs. [23, 27], we can use Eq. (58) to propose the iteration scheme as

$$\widehat{\Lambda}_{s,n+1} = (\alpha_n)^m Q\left[\widehat{\Lambda}_{s,n}\right]\,, \text{ with } \alpha_n = \frac{\int |\widehat{\Lambda}_{s,n}|^2\,\mathrm{d}k}{\int \widehat{\Lambda}_{s,n}^* Q[\widehat{\Lambda}_{s,n}]\,\mathrm{d}k}\,, \tag{59}$$

where the asterisk indicates complex conjugation and m is a free parameter that needs to be appropriately chosen for good convergence. We found empirically that the iteration scheme converges for $m > 1$, and $m = 2$ is used in all subsequent computations. A theoretical solution to the weakly nonlinear model is usually chosen as the first step of iteration, which makes the numerical comparison more convenient.

Figure 4 shows the bifurcation diagram and typical wave profiles of mode-1 solitary waves with $R_1 = 0.9$, $R_3 = 1.4$, and $h_1 = 0.3$. Mode-1 solitary waves bifurcate from $c_0^+ = 1.0412$. The amplitudes of interfaces are strictly decreasing functions versus the wave speed, where the wave amplitude is parametrized by the center displacement deviating from the equilibrium position. Both interfaces feature a single depression pulse with a monotonic decaying tail on either side of the wave trough. A comparison between numerical solutions to the strongly nonlinear model Eq. (57) and analytical solutions to the weakly nonlinear model (which are given by Eq. (55)) is presented. The weakly nonlinear model provides a good approximation for small-amplitude waves but overestimates the amplitudes of large-amplitude solutions. According to the linear theory, mode-2 solitary waves are a type of gap soliton and hence possibly exist when $c \in \left[c_0^-, c_\infty^+\right)$ (otherwise, the solitary pulse can resonate with linear waves resulting in a generalized solitary wave). Figure 5 demonstrates the results for mode-2 internal solitary waves with
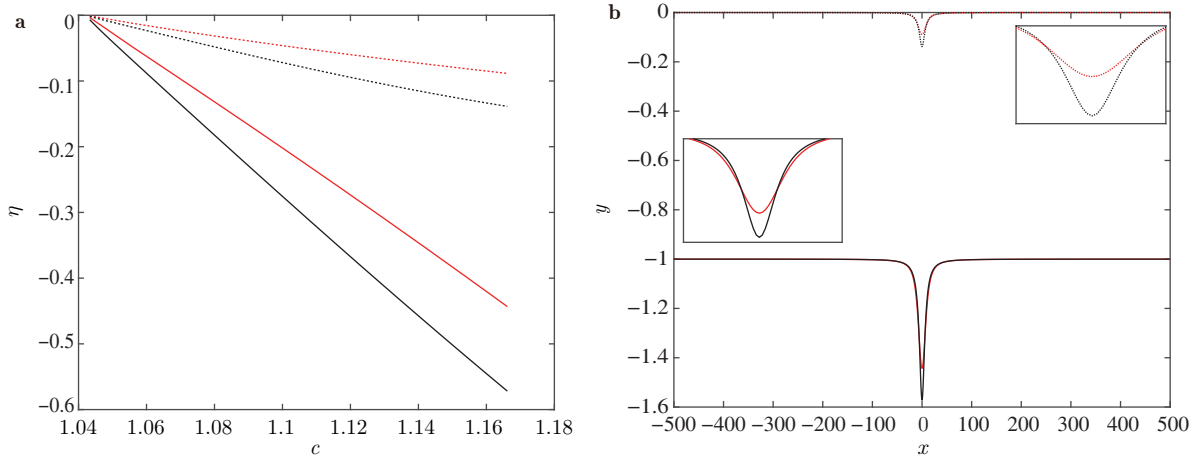
Figure 4 Mode-1 internal solitary waves computed with $R_1 = 0.9$, $R_3 = 1.4$, and $h_1 = 0.3$. **a** Speed-amplitude bifurcation curves: numerical solutions to the strongly nonlinear model (red lines); theoretical solutions to the weakly nonlinear model (black lines); upper-interface bifurcation (dotted lines); lower-interface bifurcation (solid lines). **b** Wave profiles for $c = 1.1662$; line styles are the same as **a**.
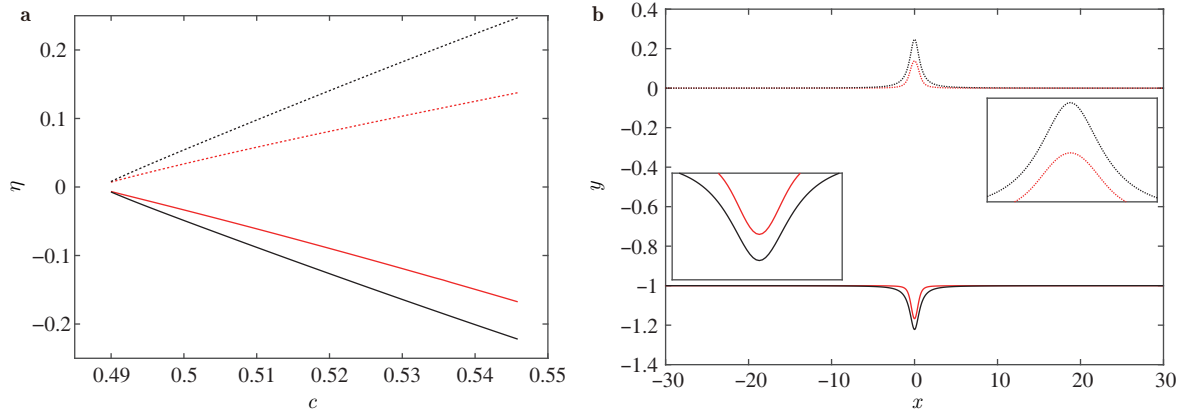
Figure 5 Mode-2 internal solitary waves computed with $R_1 = 0.6$, $R_3 = 1.4$, and $h_1 = 3$. **a** Numerical solutions to the strongly nonlinear model (red lines); theoretical solutions to the weakly nonlinear model (black lines); upper-interface bifurcation (dotted lines); lower-interface bifurcation (solid lines). **b** Wave profiles for $c = 0.5459$; line styles are the same as **a**.

$R_1 = 0.6$, $R_3 = 1.4$, and $h_1 = 3$. The mode-2 solitary waves bifurcate at $c_0^- = 0.4875$ from a free stream and exist above this threshold. Similar to the mode-1 result, the difference in wave amplitude between the numerical solutions to the strongly nonlinear model and the theoretical prediction of the weakly nonlinear model becomes significant as the wave speed increases. Mode-2 solitary waves only exist for a small range of wave speed in the strongly nonlinear model (note that $c \in [0.4875, 0.6455]$ is only a necessary condition for the existence of solitary waves). We stop the computation when the iteration diverges or oscillates and fails to reach the desired accuracy. We do not know whether solutions can fill the whole gap under this set of parameters. However, through a large number of numerical experiments, it is found that sometimes mode-2 solitary waves can exist in the strongly nonlinear model when approaching c_∞^+. A typical example for c very close to c_∞^+ is shown in Fig. 6, computed with $R_1 = 0.5$, $R_3 = 1.5$, and $h_1 = 2.1$ (such that

$c_\infty^+ \approx 0.6355$). Figure 7 shows a comparison in wave profile between mode-1 and mode-2 solutions for the same set of parameters, where the mode-1 speed, c_1, and the mode-2 speed, c_2, satisfy $c_1 - c_0^+ = c_2 - c_0^-$. As shown in this figure, the amplitude and pulse width of the mode-1 solution are more significant than the mode-2 solution, which coincides with Ref. [16]. At the same time, this comparison also testifies, to a certain extent, why the observations of mode-2 waves are less than mode-1 waves.

One of the most striking phenomena for interfacial solitary waves is the broadening of solitary pulse and the resultant conjugate flow. That is, the midsection of the interface develops a plateau that becomes infinitely long when the wave speed approaches a limiting value (see the numerical computations [22,28] in two- and three-layer fluid systems in the shallow-water regime). It is found in this work that the broad-

ening phenomenon also occurs in mode-2 solitary waves in great depth for some suitable parameters. As shown in Fig. 8, both interfaces develop into a wide platform-like structure, with the horizontal width increasing indefinitely as the wave amplitude/speed increases. We can infer from the bifurcation diagram and typical wave profiles that when the wave speed reaches a certain value, the solitary pulse of the interface starts to broaden (labeled by circles in Fig. 8a). It is noted that the upper and lower interfaces have different threshold speeds for broadening. In this example ($R_1 = 0.9$, $R_3 = 1.1$, $h_1 = 0.9$, $c_\infty^+ = 0.5000$, and $c_0^- = 0.4370$), the critical speeds are $c = 0.452094$ for the upper interface and $c = 0.451552$ for the lower interface. Both bifurcation diagrams and wave profiles show that the lower interface begins to widen before the upper interface. It is worth mentioning that, during the broadening process, both wave amplitude and speed change slightly, and therefore they are not suitable to be used as the bifurcation parameter. Instead, the area between the solitary wave and the undisturbed interface is used to continue the branch of solutions (the interested readers are referred to Ref. [28] for more details).

To confirm all these findings, we examine the existence/stability of mode-2 internal solitary waves in the fully nonlinear and non-hydrostatic Massachusetts Institute of Technology general circulation model (MITgcm), which solves the primitive Navier-Stokes equations using the finite volume method (the interested readers are referred to Ref. [29] for more details). The MITgcm model is widely used to simulate the realistic oceanic environment and check the capability of simplified theoretical equations; for instance, see cases of internal solitary waves in Ref. [30]. Here the three layers are chosen with thicknesses of $h_1 = 100\,\text{m}$,
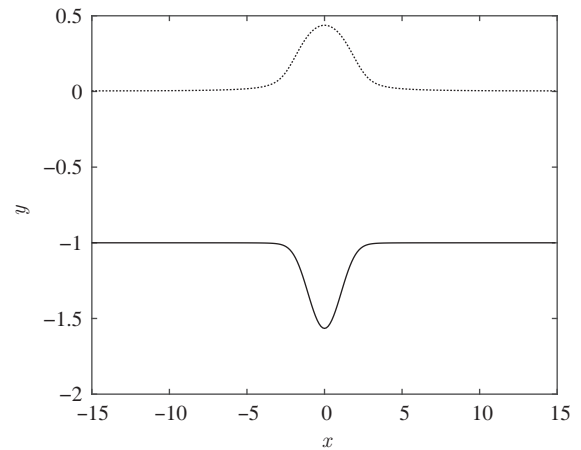
Figure 6   A mode-2 solitary wave close to $c_\infty^+ \approx 0.6355$, computed with the strongly nonlinear model for $R_1 = 0.5$, $R_3 = 1.5$, $h_1 = 2.1$, and $c = 0.6355$.
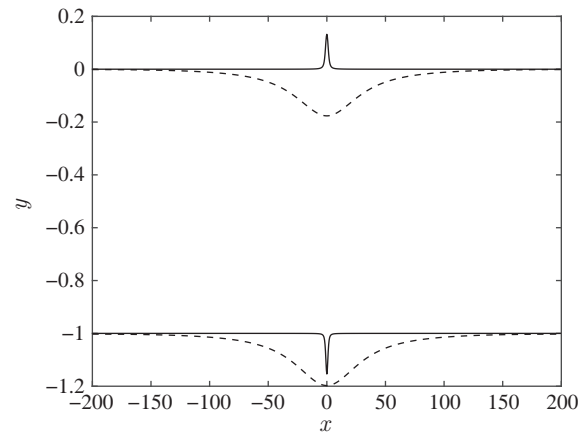
Figure 7   Mode-1 and mode-2 internal solitary waves with $R_1 = 0.7$, $R_3 = 1.3$, $h_1 = 3$, $c_0^+ = 2.1331$, and $c_0^- = 0.4852$. Mode-1 solitary wave for $c_1 = 2.1831$ (dashed line); mode-2 solitary wave for $c_2 = 0.5352$ (solid line).
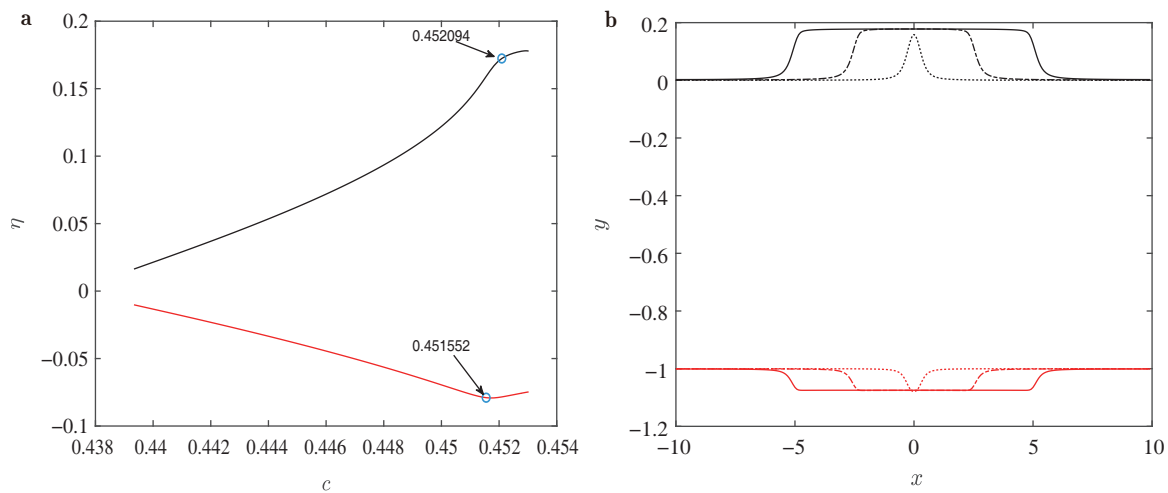
Figure 8   Pulse broadening phenomenon of mode-2 solitary waves. The parameters are chosen as $R_1 = 0.9$, $R_3 = 1.1$, and $h_1 = 0.9$. **a** Speed-amplitude bifurcation curves for the upper interface (black line) and lower interface (red line). **b** Wave profiles for $c = 0.451552$ (dotted line), $c = 0.452775$ (dash-dotted line), and $c = 0.453023$ (solid line).
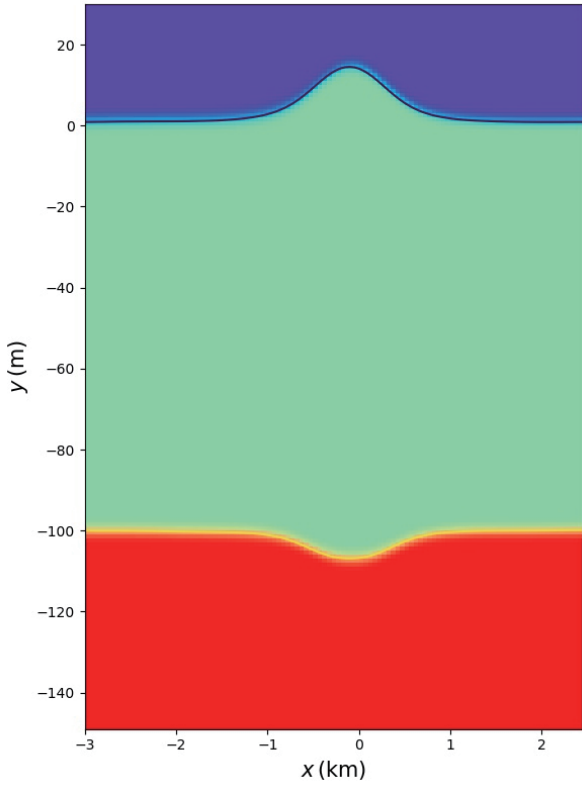
Figure 9　A stable mode-2 convex internal solitary waves in the MITgcm simulations.

$h_2 = 100\,\text{m}$, $h_3 = 1000\,\text{m}$ (an approximation to "shallow-shallow-deep") and with densities of $\rho_1 = 1000.8\,\text{kg/m}^3$, $\rho_2 = 1012.0\,\text{kg/m}^3$, $\rho_3 = 1023.3\,\text{kg/m}^3$. A theoretical solution of internal solitary waves solved in the Benjamin-Ono equation is adopted as the initial wave to launch the model. As predicted by the aforementioned theories, the mode-2 wave can survive and stably propagates forward (Fig. 9), although together with some inevitable almost imperceptible disturbances due to numerical errors.

4.　Deep-shallow-deep scenario

4.1　Strongly nonlinear model

This section derives a strongly nonlinear model in the "deep-shallow-deep" configuration, which usually happens in laboratory experiments (see Ref. [11] for example) though not very common in the real ocean. In the intermediate-long-wave regime ($h_{1,3} \gtrsim \lambda \gg h_2$) and without any assumption on wave amplitude, we use the scales in Sect. 3.1 and denote by $\mu = \frac{h_2}{\lambda}$, a parameter measuring the small dispersive effect. We follow the same procedure stated in Sect. 3.1: non-dimensionalizing the global relations and dynamic boundary conditions, expanding these expressions about the small pa-

rameter μ, and retaining terms valid up to $O(\mu)$. After a tedious calculation, one finally arrives at

$$(\eta_1 - \eta_2)_t + \nabla \cdot [(\eta_1 - \eta_2)\nabla\Phi_2] + \Delta\Phi_2 = 0\,, \tag{60}$$

$$\Phi_{2t} + D\eta_1 + \frac{1}{2}|\nabla\Phi_2|^2 + \mu R_1 G_1^{-1}\eta_{1tt} = 0\,, \tag{61}$$

$$\Phi_{2t} - (1-D)\eta_2 + \frac{1}{2}|\nabla\Phi_2|^2 - \mu R_3 G_3^{-1}\eta_{2tt} = 0\,, \tag{62}$$

where the pseudo-differential operators, G_1 and G_3, are defined in the Fourier space as

$$\widehat{G_1} = |\mathbf{k}|\tanh(|\mathbf{k}|h_1)\,, \qquad \widehat{G_3} = |\mathbf{k}|\tanh(|\mathbf{k}|h_3)\,,$$

and it is noted that $h_{1,3}$ have been non-dimensionalized by h_2. Subtracting Eq. (61) from Eq. (62) yields

$$\eta_2 = -\frac{D}{1-D}\eta_1 - \frac{\mu R_1}{1-D}G_1^{-1}\eta_{1tt}$$
$$+ \frac{\mu D R_3}{(1-D)^2}G_3^{-1}\eta_{1tt} + O(\mu^2)\,. \tag{63}$$

Eliminating η_2 in Eq. (60) by the substitution of Eq. (63), one obtains

$$0 = \eta_{1t} + (1-D)\Delta\Phi_2 + \nabla \cdot (\eta_1\nabla\Phi_2)$$
$$+ \mu\left(R_1 G_1^{-1} - \frac{DR_3}{1-D}G_3^{-1}\right)\eta_{1ttt}$$
$$+ \mu\nabla \cdot \left[\left(R_1 G_1^{-1} - \frac{DR_3}{1-D}G_3^{-1}\right)\eta_{1tt}\nabla\Phi_2\right]\,. \tag{64}$$

Equations (61) and (64) form a closed system for unknowns η_1 and Φ_2, which will be used for computing solitary waves in Sect. 4.3. Finally, we should point out that the newly developed long-wave model under the "deep-shallow-deep" scenario only supports model-2 solutions since η_1 and η_2 are of opposite signs to leading order due to the relation Eq. (63).

4.2　Weakly nonlinear models

Weakly nonlinear models include the additional expectation of small-amplitude motions. In addition to the fundamental assumption for intermediate-long waves ($h_{1,3} \gtrsim \lambda \gg h_2$), we non-dimensionalize the system by choosing the scales as Sect. 3.2. By introducing the small parameters, $\mu = \frac{h_2}{\lambda}$ and $\epsilon = \frac{a}{h_2}$, as the usual way, it is not difficult to obtain

$$\eta_{1t} - \eta_{2t} + \Delta\Phi_2 + \epsilon\nabla \cdot [(\eta_1 - \eta_2)\nabla\Phi_2] = 0\,, \tag{65}$$

$$\Phi_{2t} + D\eta_1 + \mu R_1 G_1^{-1}\eta_{1tt} + \frac{\epsilon}{2}|\nabla\Phi_2|^2 = 0\,, \tag{66}$$

$$\Phi_{2t} - (1-D)\eta_2 - \mu R_3 G_3^{-1}\eta_{2tt} + \frac{\epsilon}{2}|\nabla\Phi_2|^2 = 0\,. \tag{67}$$

We can further recast the Boussinesq-type system Eqs. (65)-(67) into a single equation by eliminating $\eta_{1,2}$. To achieve this, we take the derivative of Eqs. (66) and (67) with respect to t and eliminate η_{1t} and η_{2t} in Eq. (65). Finally, upon

noticing $\eta_1 = -\frac{\Phi_{2t}}{D} + O(\mu, \epsilon)$ and $\eta_2 = \frac{\Phi_{2t}}{1-D} + O(\mu, \epsilon)$, one obtains

$$
\Phi_{2tt} - D(1 - D)\Delta\Phi_2 - \mu[R_1(1-D)^2 G_1^{-1} \\
+ R_3 D^2 G_3^{-1}]\Delta\Phi_{2tt} + \epsilon[(|\nabla\Phi_2|^2)_t + \Phi_{2t}\Delta\Phi_2] = 0 \,, \tag{68}
$$

again a Benjamin-Ono-Benney-Luke equation.

4.3　Solitary waves

To search for solitary waves, we focus on the horizontally one-dimensional problem. Furthermore, we assume $h_{1,3} \to \infty$ for simplicity, and as a consequence, the pseudo-differential operators $G_{1,3}$ reduce to $\widehat{G}_{1,3} = |k|$. We first calculate the linear dispersion relation for the "deep-shallow-deep" scenario. Substituting $\Phi_2 = \widehat{\Phi}_2 e^{ik(x-ct)}$ into Eq. (68) and neglecting the nonlinear terms, one then obtains

$$
c^2 = \frac{D(1 - D)}{1 + \mu\left[R_1(1-D)^2 + R_3 D^2\right]|k|} \,. \tag{69}
$$

It follows directly that in contrast to the "shallow-shallow-deep" case, models for the "deep-shallow-deep" scenario only support solitary waves of a single mode, which exist for $c > c_0 = \sqrt{D(1-D)}$ (see Fig. 10 for the dispersion relation with $R_1 = 0.7$ and $R_3 = 1.1$).

　　Solitary waves in the weakly nonlinear model Eq. (68) can be solved analytically. As before, substituting $\xi = x - ct$ into Eq. (68) yields

$$
[c^2 - D(1-D)]u - \mu c^2[R_1(1-D)^2 \\
+ R_3 D^2]\mathscr{H}[u_\xi] - \frac{3\epsilon c}{2}u^2 = 0 \,, \tag{70}
$$

where $u = \Phi_{2\xi}$. Equation (70) is the steady Benjamin-Ono equation, and its solitary-wave solution has been given in Eq. (55). Finally, wave profiles of the two interfaces can be recovered from Eqs. (66) and (67).

　　On the other hand, the strongly nonlinear model, Eqs. (61) and (64), has to be solved by using the numerical iteration scheme. Substituting $\xi = x - ct$ into these two governing equations yields

$$
-cu + D\eta_1 + \frac{1}{2}u^2 + \mu c^2 R_1 \mathscr{H}\left[\eta_{1\xi}\right] = 0 \,, \tag{71}
$$

$$
(u - c)\eta_1 + (1 - D)u \\
+ \mu c^2(u - c)\left(R_1 - \frac{DR_3}{1-D}\right)\mathscr{H}[\eta_{1\xi}] = 0 \,. \tag{72}
$$

After taking the Fourier transform of Eqs. (71) and (72), we can write them in the matrix form as

$$
\widehat{X} = \widehat{\mathscr{A}}^{-1}\widehat{\mathcal{N}[X]} \,, \tag{73}
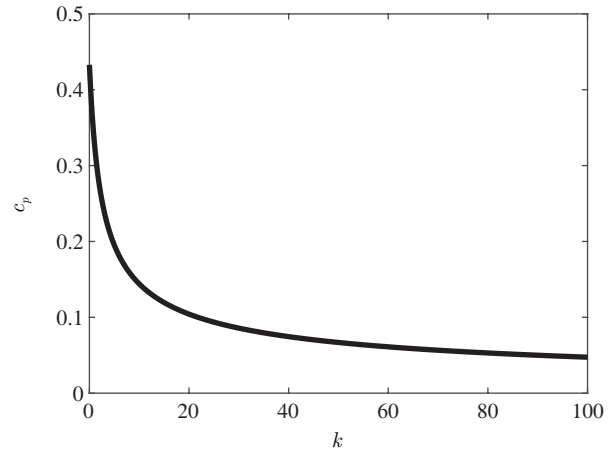$$

Figure 10　Dispersion relation Eq. (69) with $R_1 = 0.7$ and $R_3 = 1.1$.

where

$$
\widehat{\mathscr{A}} = \begin{bmatrix} D - \mu c^2 R_1 |k| & -c \\ -c + \mu c^3\left(R_1 - \frac{DR_3}{1-D}\right)|k| & 1 - D \end{bmatrix}, \quad \widehat{X} = \begin{bmatrix} \widehat{\eta_1} \\ \widehat{u} \end{bmatrix},
$$

and

$$
\widehat{\mathcal{N}[X]} = \begin{bmatrix} -\frac{1}{2}\widehat{u^2} \\ -\widehat{u\eta_1} - \mu c^2\left(R_1 - \frac{DR_3}{1-D}\right)u\widehat{\mathscr{H}\left[\eta_{1\xi}\right]} \end{bmatrix}.
$$

　　An example of solitary waves in the "deep-shallow-deep" regime is presented in Fig. 11 with $R_1 = 0.8$ and $R_3 = 1.2$, which compares the weakly (black lines) and strongly (red lines) nonlinear models. Solitary waves in the strongly nonlinear model Eq. (73) are solved numerically employing the modified Petviashvili iteration, while the corresponding solutions to the weakly nonlinear model are given by Eq. (55). Only mode-2 solitary waves are found regardless of whether the model is weakly or strongly nonlinear. Again, the analytical prediction is in good agreement with the numerical solution to the strongly nonlinear model for small-amplitude waves; however, it overestimates the wave amplitude as the wave speed increases. Finally, the pulse broadening phenomenon is not detected in our computations.

5.　Concluding remarks

Our primary focus in the current paper is modeling internal solitary waves in a three-layer fluid system of great total depth. Based on the relation between the typical wavelength and the thickness of each layer, two scenarios have been considered: the "shallow-shallow-deep" and "deep-shallow-deep" cases. Both strongly and weakly nonlinear dispersive models have been derived for the two scenarios. Horizontally one-dimensional solitary waves have been obtained analytically or numerically in these models. It is found that
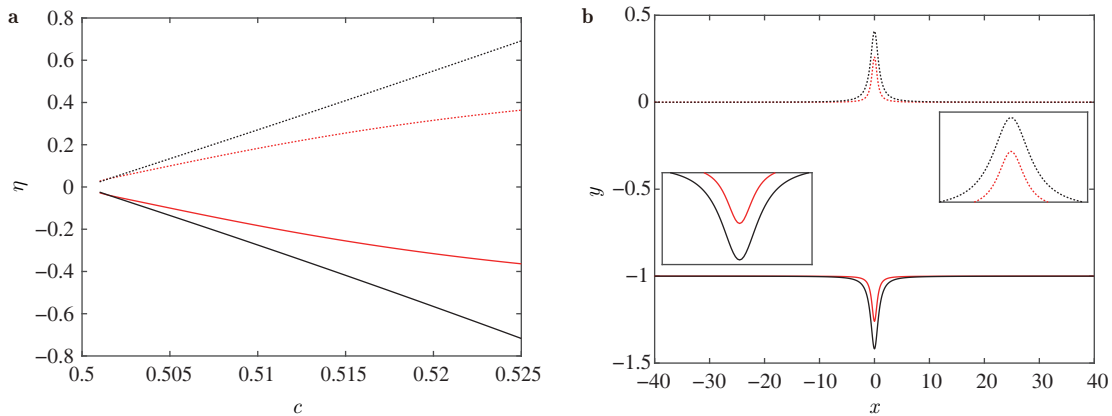
Figure 11 Mode-2 internal solitary wave in the "deep-shallow-deep" regime with $R_1 = 0.8$ and $R_3 = 1.2$. **a** Numerical solutions to the strongly nonlinear model (red lines); theoretical solutions to the weakly nonlinear model (black lines); upper-interface bifurcation (dotted lines); lower-interface bifurcation (solid lines). **b** Wave profiles for $c = 0.5150$; line styles are the same as **a**.

both mode-1 and mode-2 solitary waves exist in the shallow-shallow-deep case, but surprisingly, only mode-2 waves exist in the deep-shallow-deep models. The analytical solutions to the weakly nonlinear models agree well with the numerical solutions to the strongly nonlinear models for small-amplitude waves; however, the differences become significant as the wave amplitude increases. These theoretical predictions, particularly the existence and stability of mode-2 solitary waves, have been validated by numerically solving the primitive equations based on the MITgcm simulations. Moreover, the limiting configuration of mode-2 solitary waves, which features the infinite broadening of solitary pulse, has also been confirmed numerically by the strongly nonlinear model in the shallow-shallow-deep situation.

We have provided theoretical and numerical evidence for the existence of mode-2 internal solitary waves in deep oceans under the three-layer assumption. However, there has not been an in-depth study of the dynamics of these waves, including their generation, evolution, and dissipation mechanisms, interactions with bottom topography or mode-1 waves, flow structure when solitary waves sweep over an area, and so on. As shown in Ref. [22], multi-humped solitary waves appear along mode-2 branches in the "shallow-shallow-shallow" scenario; however, we failed to find this type of solutions when the three-fluid system is of great total depth. All the above-mentioned issues merit further investigations. On the other hand, all findings presented in this paper need to be validated by solving the full Euler equations. Finally, it is necessary to understand the hydrodynamic forces exerted by mode-2 internal solitary waves, which can provide important references for marine engineering in deep water.

1. R. B. Perry, and G. R. Schimke, Large-amplitude internal waves observed off the northwest coast of Sumatra, J. Geophys. Res. **70**, 2319 (1965).
2. A. R. Osborne, and T. L. Burch, Internal solitons in the Andaman Sea, Science **208**, 451 (1980).
3. Y. J. Yang, Y. C. Fang, T. Y. Tang, and S. R. Ramp, Convex and concave types of second baroclinic mode internal solitary waves, Nonlin. Processes Geophys. **17**, 605 (2010).
4. W. Choi, and R. Camassa, Weakly nonlinear internal waves in a two-fluid system, J. Fluid Mech. **313**, 83 (1996).
5. W. Choi, and R. Camassa, Fully nonlinear internal waves in a two-fluid system, J. Fluid Mech. **396**, 1 (1999).
6. K. R. Helfrich, and W. K. Melville, Long nonlinear internal waves, Annu. Rev. Fluid Mech. **38**, 395 (2006).
7. Y. J. Yang, Y. C. Fang, M. H. Chang, S. R. Ramp, C. C. Kao, and T. Y. Tang, Observations of second baroclinic mode internal solitary waves on the continental slope of the northern South China Sea, J. Geophys. Res. **114**, C10003 (2009).
8. J. Magalhaes, and J. da Silva, Internal solitary waves in the Andaman Sea: New insights from SAR imagery, Remote Sens. **10**, 861 (2018).
9. S. R. Ramp, Y. J. Yang, D. B. Reeder, and F. L. Bahr, Observations of a mode-2 nonlinear internal wave on the northern Heng-Chun Ridge south of Taiwan, J. Geophys. Res. **117**, C03043 (2012).
10. E. L. Shroyer, J. N. Moum, and J. D. Nash, Mode 2 waves on the continental shelf: ephemeral components of the nonlinear internal wavefield, J. Geophys. Res. **115**, C07001 (2010).
11. M. Carr, P. A. Davies, and R. P. Hoebers, Experiments on the structure and stability of mode-2 internal solitary-like waves propagating on an offset pycnocline, Phys. Fluids **27**, 046602 (2015).
12. M. Carr, M. Stastna, P. A. Davies, and K. J. van de Wal, Shoaling mode-2 internal solitary-like waves, J. Fluid Mech. **879**, 604 (2019).
13. D. Deepwell, M. Stastna, M. Carr, and P. A. Davies, Interaction of a mode-2 internal solitary wave with narrow isolated topography, Phys. Fluids **29**, 076601 (2017).
14. D. Deepwell, and M. Stastna, Mass transport by mode-2 internal solitary-like waves, Phys. Fluids **28**, 056606 (2016).
15. J. Liang, T. Du, X. Li, and M. He, Generation of mode-2 internal waves in a two-dimensional stratification by a mode-1 internal wave, Wave

Motion **83**, 227 (2018).

16　Z. Liu, R. Grimshaw, and E. Johnson, Generation of mode 2 internal waves by the interaction of mode 1 waves with topography, J. Fluid Mech. **880**, 799 (2019).

17　Z. Liu, R. Grimshaw, and E. Johnson, Resonant coupling of mode-1 and mode-2 internal waves by topography, J. Fluid Mech. **908**, A2 (2021).

18　C. Yuan, R. Grimshaw, and E. Johnson, The evolution of second mode internal solitary waves over variable topography, J. Fluid Mech. **836**, 238 (2018).

19　D. M. Farmer, and J. D. Smith, Tidal interaction of stratified flow with a sill in Knight Inlet, Deep Sea Res. Part A. Oceanogr. Res. Papers **27**, 239 (1980).

20　T. R. Akylas, and R. H. J. Grimshaw, Solitary internal waves with oscillatory tails, J. Fluid Mech. **242**, 279 (1992).

21　J. M. Vanden-Broeck, and R. E. L. Turner, Long periodic internal waves, Phys. Fluids A-Fluid Dyn. **4**, 1929 (1992).

22　R. Barros, W. Choi, and P. A. Milewski, Strongly nonlinear effects on internal solitary waves in three-layer flows, J. Fluid Mech. **883**, A16 (2020).

23　M. J. Ablowitz, A. S. Fokas, and Z. H. Musslimani, On a new non-local formulation of water waves, J. Fluid Mech. **562**, 313 (2006).

24　T. S. Haut, and M. J. Ablowitz, A reformulation and applications of interfacial fluids with a free surface, J. Fluid Mech. **631**, 375 (2009).

25　C. Yuan, Z. Wang, and X. Chen, The derivation of an isotropic model for internal waves and its application to wave generation, Ocean Model. **153**, 101663 (2020).

26　H. Ono, Algebraic solitary waves in stratified fluids, J. Phys. Soc. Jpn. **39**, 1082 (1975).

27　V. I. Petviashvili, Equation of an extraordinary soliton, Fizika Plazmy **2**, 469-472 (1976).

28　R. E. L. Turner, and J. M. Vanden-Broeck, Broadening of interfacial solitary waves, Phys. Fluids **31**, 2486 (1988).

29　J. Marshall, A. Adcroft, C. Hill, L. Perelman, and C. Heisey, A finite-volume, incompressible Navier Stokes model for studies of the ocean on parallel computers, J. Geophys. Res. **102**, 5753 (1997).

30　C. Yuan, R. Grimshaw, E. Johnson, and X. Chen, The propagation of internal solitary waves over variable topography in a horizontally two-dimensional framework, J. Phys. Oceanogr. **48**, 283 (2018).

大深度三层流体中的海洋内孤立波

王梓安, 王展, 袁春鑫

摘要　　本文致力于研究深海非线性内波. 将海洋抽象为由三种流体构成的具有稳定密度层结的系统. 基于无旋流动的Ablowitz-Fokas-Musslimani公式, 我们对"浅水-浅水-深水"和"深水-浅水-深水"两种情形建立新的强非线性和弱非线性模型, 并详细比较了不同模型中内孤立波波形及"速度-振幅"的全局分叉图. 对于"浅水-浅水-深水"情形, 可以获得一模态和二模态两种类型的内孤立波, 并且在二模态内波中观察到脉冲展宽现象及其极限形态—共轭流. 然而对于"深水-浅水-深水"情形, 只能得到二模态内孤立波. 基于MITgcm求解原始方程, 我们证实了深海中二模态内波的存在性和稳定性.